Chinese Chemical Letters 34 (2023) 108318

Contents lists available at ScienceDirect

Chinese Chemical Letters

journal homepage: www.elsevier.com/locate/cclet

MOF-derived heterostructure CoNi/CoNiP anchored on MXene framework as a superior bifunctional electrocatalyst for zinc-air batteries

Jingyuan Qiao[a], Zhuoheng Bao[a], Lingqiao Kong[a], Xingyu Liu[a], Chengjie Lu[a], Meng Ni[b], Wei He[a,*], Min Zhou[c,*], ZhengMing Sun[a,*]

[a] *Jiangsu Key Laboratory of Advanced Metallic Materials, School of Materials Science and Engineering, Southeast University, Nanjing 211189, China*
[b] *Department of Building and Real Estate, Research Institute for Sustainable Urban Development (RISUD) and Research Institute for Smart Energy (RISE), The Hong Kong Polytechnic University, Hong Kong 999077, China*
[c] *School of Chemistry and Materials Science, University of Science and Technology of China, Hefei 230026, China*

ARTICLE INFO

Article history:
Received 15 November 2022
Revised 7 February 2023
Accepted 7 March 2023
Available online 12 March 2023

Keywords:
Heterostructure
Metal-organic frameworks
MXene
Bifunctional electrocatalyst
Zn-air battery

ABSTRACT

Zinc-air batteries (ZABs) are regarded as promising next-generation energy storage devices but limited by their sluggish oxygen reduction/evolution reactions (ORR/OER). Herein, the bifunctional catalyst consisting of MXene and metal compounds has been constructed *via* a controllable strategy. For demonstration, a 3D MXene framework with anchored heterostructure CoNi/CoNiP and nitrogen-doped carbon (NC) called H-CNP@M is constructed by metal-ion inducement and phosphorization. The bimetal-semiconductor heterostructure greatly enhances the catalytic performance. The H-CNP@M exhibits superior activities toward ORR ($E_{1/2} = 0.833$ V) and OER ($\eta_{10} = 294$ mV). Both aqueous and all-solid-state ZAB assembled with H-CNP@M demonstrate superior performance (peak power density of 166.5 mW/cm^2 in aqueous case). This work provides a facile and general strategy to prepare MXene-supported bimetallic heterostructure for high-performance electrochemical energy devices.

Rechargeable zinc-air batteries (ZABs) are deemed to be one of the most promising energy storage systems due to their high energy density, high safety, and low cost [1]. However, the slow kinetics of the oxygen evolution reaction (OER) and oxygen reduction reaction (ORR) on the cathode impede their large-scale practical applications [2]. Usually, noble metals and their derivatives, such as Pt, IrO_2, and RuO_2, demonstrate efficient catalytic activity. However, low reserves, high cost, and rapid deactivation limit the wide application of noble metal-based catalysts [3]. Thus, developing low-cost, highly active, and stable bifunctional catalysts is of great significance. Transition metal compounds and their heterostructure hybrids have attracted great interest in recent years due to their low cost and favorable catalytic performance [4,5]. The strong interfacial bonding between hetero-structured materials leads to the rearrangement of electrons, thereby optimizing the adsorption of reactants and resulting in excellent catalytic activity [6,7]. However, transition metal compounds and heterostructure hybrids also suffer from agglomeration during the synthesis and test processes, which greatly reduces the specific surface area and impedes the applications of the catalysts [8,9].

Recently, metal-organic frameworks (MOFs) with different metal centers have exhibited excellent compatibility, showing a simple way to synthesize homogenous multi-metallic MOF crystals [10,11]. MOF-derived composites obtained through pyrolysis demonstrate favorable intrinsic electrocatalytic activity, high electric conductivity, and large specific surface area due to the homogenous dispersion of metallic active sites on carbon [12,13]. In addition, the flexible regulation of post-treatment according to demand facilitates the design of multifunctional catalysts. For example, the bimetallic Co/Cu-embedded N-doped carbon structure derived from CoCu-MOFs demonstrates the impressively trifunctional activity in alkaline [14]. And the CoP@FeCoP with a yolk-shell structure synthesized *via* the phosphorization of ZIF-67@Co-Fe Prussian blue analogs showed low overpotentials for both hydrogen evolution reaction (HER) and OER (141 and 238 mV respectively, at 10 mA/cm^2) [15]. The MOF derivatives discussed above are all obtained by the pyrolysis process. However, the original pore structure collapses during pyrolysis and hinders mass transfer during electrocatalysis, and the carbon graphitization degree is not ef-

---

* Corresponding authors.
E-mail addresses: weih@seu.edu.cn (W. He), mzchem@ustc.edu.cn (M. Zhou), zmsun@seu.edu.cn (Z. Sun).

https://doi.org/10.1016/j.cclet.2023.108318

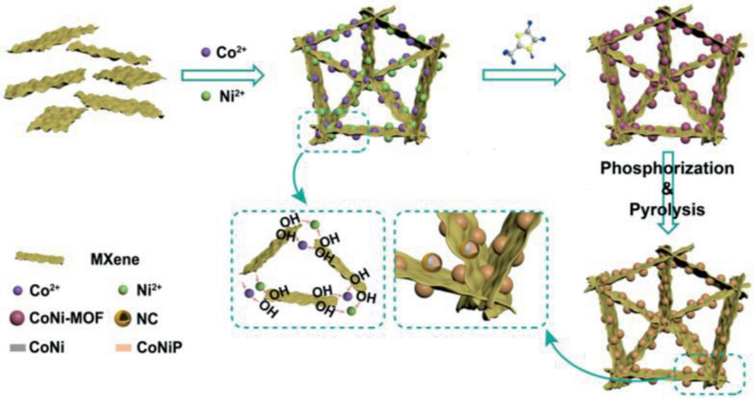

Fig. 1. Schematic illustration of the fabrication of H-CNP@M.

ficient, which leads to low electrical conductivity and poor structural stability [13]. It has been reported that the porous structure of nitrogen-doped carbon is of significance for catalysis, and a 3D macro- and mesoporous structure exhibits preferable mass transfer properties and electrochemical activity [16]. Therefore, a 3D porous framework with high electrical conductivity, proper pore structure, and large surface area is necessary for loading these MOF derivatives.

MXenes, a novel family of 2D transition metal carbides and/or nitrides, demonstrate metal conductivity, hydrophilicity, numerous functional groups, and ultralow work function [17]. 2D MXene nanosheets have been explored as catalysts and substrates in water splitting and metal-air batteries with superior electrochemical activity [18]. However, the agglomeration of MXene nanosheets alleviates the mass transfer and reduces the electrochemical activity. Fabrication of 3D macroscopic MXene framework is effective to reduce the self-restacking or agglomeration [19–21]. Furthermore, because of the functional groups, a 3D MXene framework can be easily constructed through a gelation process triggered by metal ions, which provides a good platform for hybrid catalysts with special structures and strong interfacial interactions [22].

Inspired by the above discussions, we controllably constructed bimetallic-based compounds on MXenes *via* facile metal-ion-induced self-assembly and heat treatment. Specifically, the metal ions trigger MXene to form a 3D porous framework and act as centers for the *in-situ* growth of bimetallic MOFs (MOFs@MXene). And after the post-procedure, a special structure with 3D porous MXene frameworks as the carrier to support carbon coupled with the bimetallic compounds. Co^{2+} and Ni^{2+} are used to trigger MXene as a representative to prepare CoNi-MOFs@MXene. And after phosphorization, the designed structure H-CNP@M is obtained. The prepared hybrid catalyst with a heterostructure demonstrates bifunctional catalytic activity (ORR and OER) that can be attributed to the synergistic effect of the CoNi/CoNiP heterostructure. Meanwhile, the unique 3D structure with a hierarchical pore structure exposes more active sites while also greatly promoting mass transfer. Thus, H-CNP@M exhibits a comparable ORR activity with commercial Pt/C and low overpotentials for OER. And given the excellent bifunctional activity, the H-CNP@M catalyst shows promising potential for the application of the liquid and flexible rechargeable Zn-air batteries.

The synthesis procedure of H-CNP@M is illustrated in Fig. 1. The aqueous solution containing equal amounts of $Co(NO_3)_2$ and $Ni(NO_3)_2$ was slowly dropped into the $Ti_3C_2T_x$ dispersion (~5 mg/L), which was obtained by the common etching method [23]. The metal ions destroyed the electrostatic repulsion between the MXene nanosheets and cross-linked with the -OH groups of MXene to form a stable 3D MXene framework (Fig. S1a in Supporting information). Then, an aqueous solution of 2-methylimidazole was slowly added to the above mixture with stirring to grow CoNi bimetallic MOFs *in situ* on the MXene framework (CoNi-MOFs@MXene, the microstructure is shown in Fig. S1b in Supporting information). The microstructure of CoNi-MOFs without MXene is shown in Fig. S1c (Supporting information). After carbonization and phosphorization, H-CNP@M was obtained (Fig. S1d in Supporting information). For comparison, CN@M was obtained by a similar method excluding the phosphorization process. CN and H-CNP without the addition of MXene were synthesized through pyrolysis and pyrolysis-phosphorization, respectively. CNP and CNP@M were synthesized by increasing the amount of phosphorus source.

The phase of the CoNi-MOFs@MXene precursor is shown in Fig. S2a (Supporting information). There are only peaks corresponding to the CoNi-MOF and MXene in the precursors, and no unexpected phase exists. The (002) peak of MXene in the CoNi-MOFs@MXene shifts slightly to a lower angle, which may be due to the intercalation of metal ions between the MXene layers resulting in a larger interlayer spacing [22]. Fig. 2a and Fig. S2b (Supporting information) present the XRD patterns of the synthesized samples, and the characteristic peaks at approximately 6.2° of MXene are found in all MXene-containing samples, CN@M, CNP@M and H-CNP@M, indicating favorable stability of the MXene framework after pyrolysis and phosphorization. After carbonization, the samples deliver a broad peak between 20° and 30° and sharp peaks at approximately 44.3° and 51.7°, which can be assigned to the carbon and the (111) and (200) planes of CoNi (PDF #01-074-5694), respectively. Furthermore, in addition to the abovementioned CoNi diffraction peaks, the samples after phosphorization show new peaks at approximately 41°, 44.9°, and 47.6°, which coincide with the (111), (201), and (210) planes of CoNiP (PDF #04-001-6153), respectively. The corresponding element mapping analysis of H-CNP@M confirms the uniform distribution of Co, Ni, P, N, and Ti elements, indicating successful phosphorization and dispersion of phases (Fig. S3 in Supporting information).

The 3D MXene framework is well preserved after pyrolysis and phosphorization from the SEM image of H-CNP@M (Fig. S1d). And the higher magnification SEM image (Fig. 2b) shows that the CoNi-MOF-derived nanoparticles with homogenous distribution are anchored on the MXene nanosheets, which indicates that the MXene may efficiently avoid the agglomeration of nanoparticles [24]. To further analyze the microstructure and phase components of H-CNP@M, TEM was carried out. As shown in Fig. 2c and Fig. S4a (Supporting information), numerous particles with a uniform size of 10–50 nm are evenly distributed on the MXene framework, which is consistent with the SEM images. Meanwhile, the nanopores in the MXene nanosheets are observed (Fig. 2c), which may provide additional pathways for the diffu-

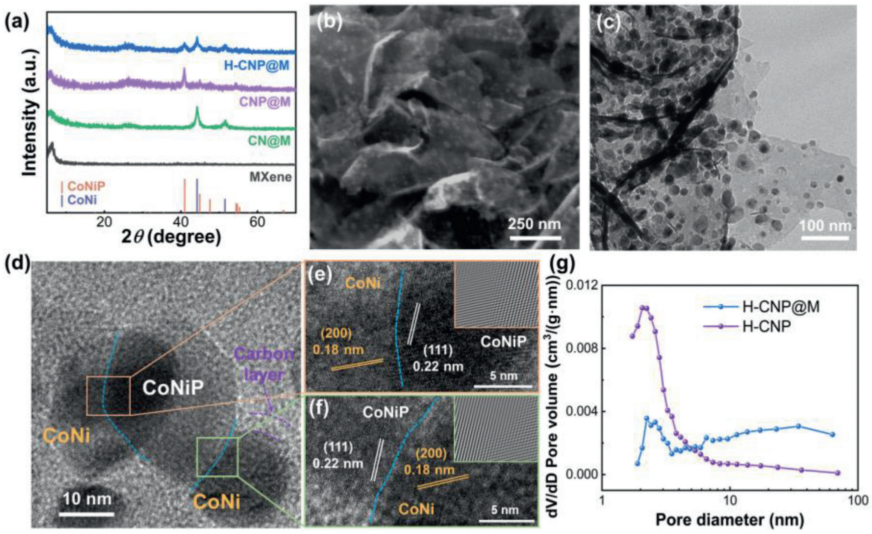

Fig. 2. (a) XRD patterns of MXene, CN@M, CNP@M, and H-CNP@M. (b) SEM image, (c) TEM image, and (d-f) HRTEM images of H-CNP@M, the insets in (e) and (f) are the filtered IFFT images. (g) The pore-size distribution of H-CNP@M and H-CNP.

sion of reactants [25,26]. And high-resolution transmission electron microscopy (HRTEM) further illustrates that nanoparticles wrapped in the nitrogen-doped carbon layer are supported on MXene nanosheets (Fig. S4b in Supporting information). More importantly, in the energy-dispersive X-ray spectrometry (EDX) mappings (Figs. S4c and d in Supporting information), the Co and Ni uniformly disperse through the entire architecture of the nanocrystals on MXene nanosheets but the phosphorus element does not appear in some of the particles, which confirm the formation of the CoNi/CoNiP heterostructure. And the lattice mismatches are also observed in the enlarged image, as shown in Fig. 2d. The lattice fringes with spacings of 0.18 nm and 0.22 nm correspond to the (200) plane of CoNi and the (111) plane of CoNiP, respectively (Figs. 2e and f). The corresponding magnified inverse fast Fourier transform (IFFT)-filtered images (inset of Figs. 2e and f) clearly show the mismatched lattices, and further clearly confirm the heterostructure of CoNi/CoNiP. The formation of a heterostructure may be accompanied by fast interfacial charge transfer and charge rearrangement, showing enhanced catalytic performance. Meanwhile, the microstructure and specific surface area of the H-CNP@M were further analyzed by N_2 adsorption/desorption experiments. As shown in Fig. S5 (Supporting information), H-CNP@M displays a type II isotherm, indicating a mesoporous structure [27], and possesses a specific surface area of 70 m^2/g, which is higher than that of H-CNP (58 m^2/g). The pore-size distribution demonstrates that H-CNP@M has a meso-macropore structure which is different from that of H-CNP (Fig. 2g). The superior BET surface area and hierarchical pore structure can expose more active sites and facilitate the diffusion of reactants and products, which is conducive to the kinetics of the reaction.

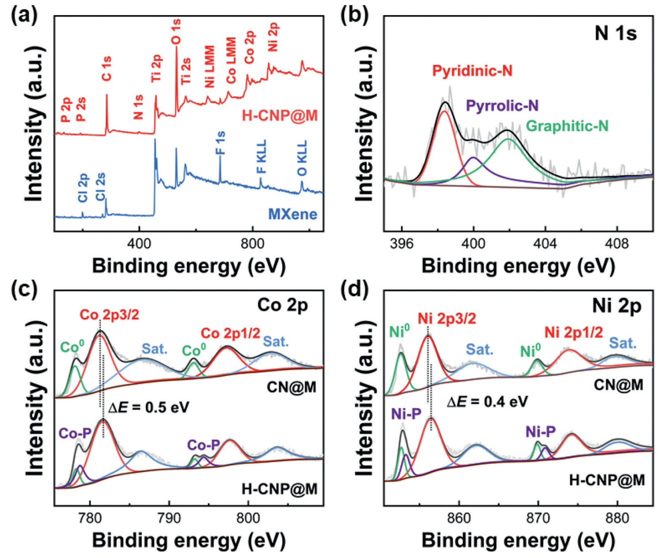

Fig. 3. XPS survey spectrum (a) and high-resolution XPS spectrum of (b) N 1s, (c) Co 2p and (d) Ni 2p before and after phosphorization.

The XPS was performed to further analyze the chemical composition and corresponding chemical bonding of the samples. Fig. 3a presents the XPS survey spectrum, which displays the presence of Ti, Co, Ni, P, N, and C, corresponding to the EDX results. The high-resolution N 1s spectrum (Fig. 3b) can be deconvoluted into pyridinic-N (398.4 eV), pyrrolic-N (400.0 eV), and graphitic-N (401.9 eV) [28]. Pyridinic-N and graphitic-N are highly effective actives to boost both ORR and OER activity, and the high content of them in H-CNP@M may benefit the ORR/OER performance [28–30]. From the high-resolution P 2p spectrum (Fig. S6 in Supporting information), the peaks at 129.8 and 130.6 eV are close to the binding energies of P $2p_{1/2}$ and P $2p_{3/2}$ in CoNiP, respectively. Additionally, the broad peak at 133.6 eV can be assigned to oxidized phosphorus species, which may be attributed to air contact [7,31,32]. Fig. 3c presents the high-resolution Co 2p spectra of CN@M and H-CNP@M. For CN@M, the spectrum can be well deconvoluted into metallic Co (Co^0), oxidized Co species (Co^{2+}), and a couple of associated satellite peaks (sat.). It is worth noting that the peaks of Co species in Co-P appear at 778.9 and 794.2 eV in the spectrum of H-CNP@M [33,34]. More importantly, the binding energy of Co^{2+} in H-CNP@M positively shifts by 0.5 eV compared with that in CN@M, implying a change in the Co^{2+} electronic microenvironment after phosphorization. Similarly, in the Ni 2p spectrum of H-CNP@M (Fig. 3d), the binding energies of 853.3 and 870.9 eV are assigned to $Ni^{\delta+}$ in the Ni-P compound, and the doublets at approximately 856.4 and 874.2 eV accompanied by two satellites at 862.1 and 879.9 eV are attributed to Ni $2p_{3/2}$ and $2p_{1/2}$ in oxidized Ni, respectively [24]. The binding energy of Ni^{2+} $2p_{3/2}$ in H-CNP@M positively shifts by 0.4 eV compared with that in CN@M, indicating the formation of metal-P bonds. The above results suggest the successful synthesis of the heterostructure of CoNi-CoNiP, which is supported by NC and MXene.

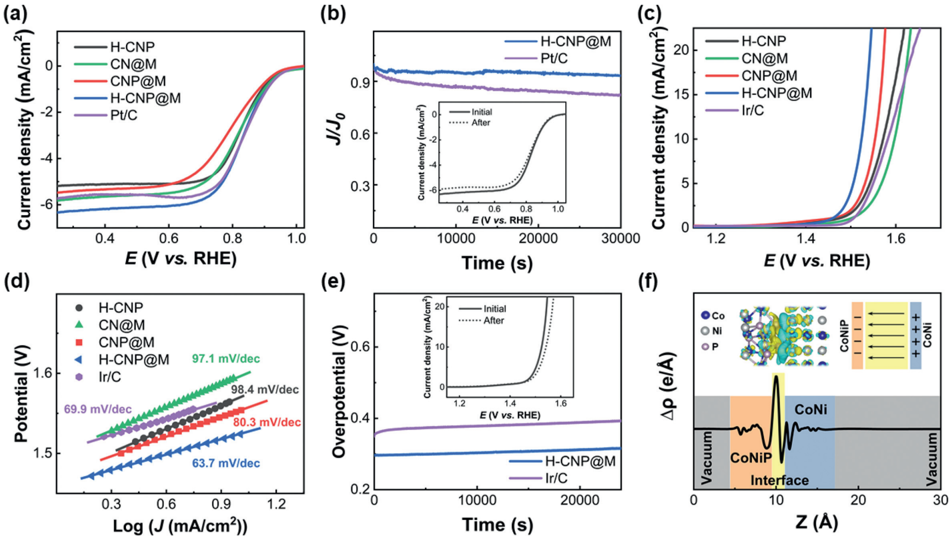

Fig. 4. (a) ORR curves of catalysts in O_2-saturated 0.1 mol/L KOH solution at 1600 rpm. (b) ORR chronoamperometric curves of H-CNP@M and Pt/C at constant potentials of 0.6 V. (c) OER curves for different catalysts at 1600 rpm in N_2-saturated 0.1 mol/L KOH. (d) Tafel slopes. (e) OER chronopotentiometry curves at 10 mA/cm^2 of H-CNP@M and Ir/C. (f) Charge density difference for CoNi/CoNiP heterostructure.

The bifunctional oxygen electrocatalysis performance of H-CNP@M and the compared samples were all evaluated in 0.1 mol/L KOH by a typical three-electrode system with Hg/HgO as the reference electrode and a graphite rod as the counter electrode. The linear sweep voltammetry (LSV) curves of the as-synthesized catalysts and Pt/C obtained at 1600 rpm in 0.1 mol/L KOH are shown in Fig. 4a and Fig. S7a (Supporting information). H-CNP@M shows the best ORR activity among all the samples with a half-wave potential ($E_{1/2}$) of 0.833 V, which is only 10 mV lower than that of Pt/C and much better than that of the other as-synthesized catalysts and reported transition metal phosphides (TMPs) (details are shown in Table S2 in Supporting information). More importantly, the mixed MXene and CoNi/CoNiP@NC (H-CNP + M) shows no significant difference in performance from H-CNP (Fig. S7a) which fully illustrates the importance of 3D MXene frameworks and *in situ* growth. Since the MXene framework facilitates the mass transfer of the reactants, H-CNP@M, CN@M, and CNP@M show impressive diffusion-limiting current densities of 6.1, 5.6 and 5.3 mA/cm^2, respectively, which are comparable with commercial Pt/C (5.5 mA/cm^2) and higher than those of other samples without MXene and some reported TMP catalysts (Table S2 in Supporting information). To further investigate the kinetics of H-CNP@M, the corresponding Tafel slope and the LSV curves at different rotating speeds ranging from 400 rpm to 2500 rpm were obtained (Figs. S7b-d in Supporting information). The Koutecky-Levich (K-L) plots for potentials ranging from 0.3 V to 0.6 V are almost parallel (inset of Fig. S7b), indicating that oxygen reacts *via* first-order reaction kinetics with the concentration of dissolved O_2. The corresponding electron transfer numbers (n) of H-CNP@M are close to the theoretical value of 4, demonstrating the efficient four-electron pathway [35]. And the lowest Tafel slope (98.5 mV/dec) suggests the dramatically accelerated ORR kinetics of H-CNP@M. The superior ORR performance of H-CNP@M may be attributed to its unique 3D structure coupled with the TMP-based heterostructure, which accelerates O_2 diffusion and charge transfer. Moreover, H-CNP@M demonstrates high current retention of 94% after 30,000 s, which is much higher than that of commercial Pt/C (80%), as shown in Fig. 4b.

The OER is of importance as a half-reaction in zinc-air batteries. Therefore, the OER performance of H-CNP@M was also investigated using a rotating disk electrode in 0.1 mol/L KOH. Fig. 4c and Fig. S7e (Supporting information) show the iR-compensated LSV curves of the as-synthesized samples and Ir/C. Among the catalysts, H-CNP@M shows the lowest overpotential of 294 mV at 10 mA/cm^2, which is significantly lower than Ir/C and some other reported TMP-based catalysts, such as CoP@PNC-DoS (316 mV, 0.1 mol/L KOH) [36] and Co_2P/CoNPC (326 mV, 1 mol/L KOH) [37]. A detailed comparison of the reported catalysts is presented in Table S3 (Supporting information). And the mixed simple (H-CNP + M) does not exhibit similar excellent performance as H-CNP@M (Fig. S7e). Moreover, the smallest Tafel slope of H-CNP@M (63.7 mV/dec) reveals the fastest OER kinetics (Fig. 4d and Fig. S7f in Supporting information) [7,38]. The results above suggest that the heterostructure and 3D MXene framework with a hierarchical structure may accelerate electron transfer and provide smooth paths for reactant diffusion, thereby significantly enhancing OER kinetics. Furthermore, the unique MXene framework also leads to an increase in the electrochemically active surface area (ECSA). The ECSA is usually estimated from the double-layer capacitance (C_{dl}) since the double-layer capacitance is proportional to the ECSA. As shown in Fig. S8 (Supporting information), H-CNP@M has a C_{dl} (20.6 mF/cm^2) that is much larger than that of H-CNP (13.4 mF/cm^2). The larger ECSA of H-CNP@M implies that the unique 3D structure with a hierarchical pore structure greatly enlarges the exposure of active sites and thus promotes the OER performance. Apart from activity, durability is another important performance factor of the OER. As shown in Fig. 4e, the overpotential of H-CNP@M at 10 mA/cm^2 only shifted approximately 15 mV after 24000 s, which is significantly better than Ir/C (40 mV). Impressively, H-CNP@M shows a small potential gap of 0.691 V between the OER and ORR ($\Delta E = E_{j10} - E_{1/2}$), which is superior to Pt/C + Ir/C, other as-synthesized samples (Fig. S9 in Supporting information), and most of the recently reported bifunctional oxygen electrocatalysts (Table S4 in Supporting information). The excellent bifunctional activity of H-CNP@M is attributable not only to the form of the heterostructure but also to the highly exposed active sites and smooth paths of reactant diffusion, which are the results of the hierarchical structure.

It is reported that the heterostructure is of importance for the oxygen catalysis [6,7,39,40]. To further understand the mechanism of improved bifunctional oxygen catalysis, a model of CoNi/CoNiP heterostructure is established. The lattice constants of cubic CoNi are $a = b = c = 3.52$ Å with space group of Fm-3m, and those of bulk CoNiP are $a = 5.83$ Å, $b = 5.83$ Å, $c = 3.35$ Å with space group of P-62m, which is consistent with the XRD data. The CoNi (200)

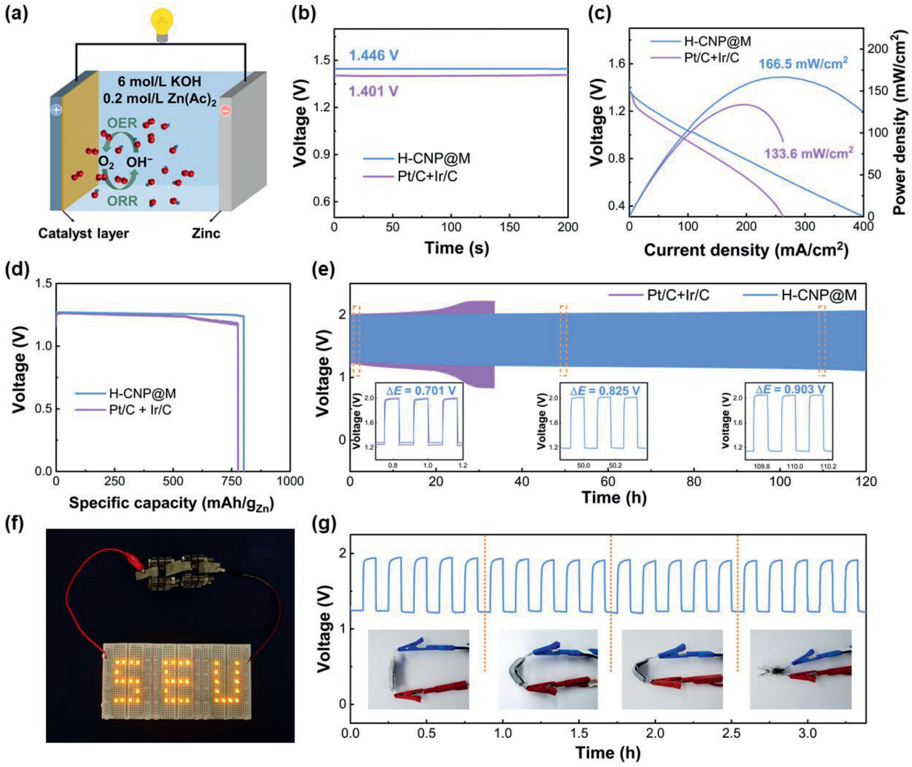

Fig. 5. (a) Schematic illustration of the homemade liquid Zn-air battery. (b) The open-circuit voltage of ZABs. (c) The discharge polarization curves and the corresponding power density of ZABs. (d) The specific capacity of ZABs at 10 mA/cm^2. (e) Galvanostatic discharge-charge cycling curves at 10 mA/cm^2 of the liquid ZABs. (f) The digital photograph of the "SEU" LED logo lighted by two H-CNP@M-based ZABs in series. (g) Galvanostatic discharge-charge cycling curves at 1.0 mA/cm^2 under different bending states.

plane and the CoNiP (111) plane were selected to construct a heterojunction model according to the experiment results. And Fig. S10 (Supporting information) shows the atomic models of CoNi, CoNiP, and CoNi/CoNiP. As shown in Fig. S11a (Supporting information), the work functions of CoNi and CoNiP are different and the Fermi level of CoNi is within the bandgap of CoNiP. When the Mott-Schottky contact forms (Fig. S11b in Supporting information), both conduction and valence bands of CoNiP are bent downward, providing a fast path for the electrons transfer. And the electrons spontaneously transfer from CoNi to CoNiP across the heterointerface to equate the Fermi levels of both and result in the redistribution of electrons and the form of the built-in electric field. And the interfacial charge transfer between CoNi and CoNiP is further verified by the charge density difference (Fig. 4f). As shown in the inset of Fig. 4f, at the interface between CoNi and CoNiP, the CoNi part is mainly covered by the cyan, which indicates charge depletion. Meanwhile, the yellow region locates on the CoNiP represents charge accumulation. The increased electron density of the CoNiP side may reduce the adsorption and/or desorption barriers for the reaction intermediates, thus promoting the OER performance [6,41]. And the CoNi side also optimizes the adsorption energy of oxygen due to the electron redistribution. Usually, the d-band center is an important factor to determine the intrinsic oxygen catalysis activity. And as shown in Fig. S11c (Supporting information), the d-center of CoNi/CoNiP heterostructure upshift to −1.13 eV which is beneficial to enhancing the adsorption of reaction intermediates. The properly upshifted d-band center can reduce the electron filling of the antibonding states and then optimize the bond strength between the catalytic surface and intermediates species, which can greatly facilitate charge transfer and exhibit outstanding bifunctional activity [42,43]. These results demonstrate that the Mott-Schottky effect in CoNi/CoNiP can result in electron redistribution, thereby providing a highway for electron transfer and enhancing the utilization of active sites to exhibit excellent bifunctional activity [44].

The composition and morphology of H-CNP@M after the durability test of the ORR and OER were checked by XRD and TEM. Fig. S12 (Supporting information) demonstrates the XRD patterns of the samples after the ORR and OER durability tests. The XRD pattern for the sample after the ORR remains the same as that before the test, indicating the excellent durability of H-CNP@M. However, the peaks of CoNiP are weakened after the durability test of the OER, which may be attributed to hydroxide/oxide formation on the surface of metal phosphides [36]. The morphology and microstructure of H-CNP@M after the ORR and OER durability tests were further studied (Figs. S13 and S14 in Supporting information). There is no significant morphological change observed after the durability test of the ORR and OER. The MXene architecture is well preserved, and the nanoparticles are also homogeneously distributed, like the initial sample, which is confirmed by the EDX mapping results. Furthermore, in the HRTEM images of the sample after the ORR and OER tests, the CoNi/CoNiP heterostructure is also retained with clear lattice fringes. But the new lattice fringes can be observed in the HRTEM image of the sample after the OER test, which may belong to the hydroxide/oxide species of Co and/or Ni and correspond to the weakening of the diffraction peak intensity of phosphide species in XRD [36].

Considering the excellent bifunctional catalytic activities, H-CNP@M is employed as an air cathode of a homemade rechargeable liquid Zn-air battery (Fig. 5a), and Pt/C + Ir/C with a mass ratio of 1:1 is chosen as a reference. Impressively, the Zn-air battery with the H-CNP@M cathode delivers a higher open-circuit voltage of 1.446 V than that of Pt/C + Ir/C (1.401 V), as shown in Fig. 5b, and it is also much higher than some recently reported TMP-based ZABs, such as Co_2P/CoNPC (1.425 V) [37], CoO/Co_xP (1.4 V) [7] and Co_2P@NPC (1.43 V) [29]. The small voltage changes in the galvanostatic discharge measurements at different current densities from 1 mA/cm^2 to 50 mA/cm^2 demonstrate good rate performance (Fig. S15 in Supporting information). Additionally, as shown in Fig. 5c, a maximum power density of 166.5 mW/cm^2 is obtained in the H-CNP@M ZAB, which is higher than that of the Pt/C + Ir/C cathode (133.6 mW/cm^2). This value exceeds many recently reported bifunctional electrocatalysts, such as Co_2P/CoNPC (116 mW/cm^2) [37], In-CoO/CoP heterostructure (139.4 mW/cm^2) [45], CoO/Co_xP (122.73 mW/cm^2) [7] and CuCoP-NC-700 (116.5 mW/cm^2) [46]. A detailed comparison related more reported catalysts is shown in Table S5 (Supporting information). Fig. 5d delivers the galvanostatic discharge specific capacity of H-CNP@M (801 mAh/g), which also surpasses that of Pt/C + Ir/C (776 mAh/g). Furthermore, at 10 mA/cm^2, the initial charge-discharge voltage gap of H-CNP@M is 0.701 V, and the slight increment of the voltage gap after the continuous work of 120 h reflects the outstanding cyclic stability (Fig. 5e). The 40 light-emitting diode lights can be powered by two ZABs connected in series (Fig. 5f), manifesting its possibility in practical applications.

Inspired by the development of flexible energy storage devices, a homemade flexible ZAB is fabricated with H-CNP@M spayed on carbon cloth as the air cathode, alkaline gel of polyvinyl alcohol (PVA/KOH) as the electrolyte, and Zn plate as the anode. Impressively, the flexible ZAB catalyzed by H-CNP@M obtains a high open-circuit voltage of 1.398 V, which is obviously better than that of the flexible ZAB based on Pt/C + Ir/C (Fig. S16a in Supporting information). As shown in Fig. S16b (Supporting information), it also exhibits a remarkable peak power density of 45 mW/cm^2, which is higher than that of many previously reported flexible ZABs, such as Ru-RuO_2 (29 mW/cm^2) [39], N-GQDs/$NiCo_2S_4$/CC (26.2 mW/cm^2) [38], FeP/Fe_2O_3@NPCA (40.8 mW/cm^2) [47] and FeCoNi-NC (39.7 mW/cm^2) [48]. And the as-prepared flexible ZAB can exhibit a stable charge/discharge voltage (~1.92 V/~1.22 V) at 1 mA/cm^2. Impressively, the charge/discharge voltage of flexible ZAB has no significant change even bent from 0° to 180° (Fig. 5g). This indicates that the as-prepared flexible Zn-air battery has excellent flexibility and is promising for future flexible electronic devices.

In summary, a MXene-based hierarchical pore structure containing CoNi/CoNiP heterostructure called H-CNP@M was successfully synthesized. The fast interfacial electron transfer and the rearrangement of electrons of the heterostructure lead to excellent intrinsic bifunctional activity. Thus, H-CNP@M exhibits a high half-wave potential of the ORR (0.833 V) and low overpotential and Tafel slope of OER (294 mV at 10 mA/cm^2, 63.7 mV/dec). H-CNP@M also presents a high peak power density of 166.5 mW/cm^2 and good cycle stability when assembled into Zn-air batteries. This work provides a simple strategy for constructing MXene-supported heterostructure for electrochemical energy storage applications.

Declaration of competing interest

The authors declare that they have no known competing financial interests or personal relationships that could have appeared to influence the work reported in this paper.

Acknowledgments

This study was supported by Natural Science Foundation of Jiangsu Province (No. BK20200406), National Natural Science Foundation of China (Nos. 51731004, 22075263, 52002366), National Key R&D Program of China (No. 2021YFA1501502), the Fundamental Research Funds for the Central Universities (No. WK2060000039), the Collaborative Research Fund (No. C5031-20G) from Research Grant Council, University Grants Committee, Hong Kong SAR, and Project of Strategic Importance Program of The Hong Kong Polytechnic University (No. P0035168).

Supplementary materials

Supplementary material associated with this article can be found, in the online version, at doi:10.1016/j.cclet.2023.108318.

References

[1] S. Wang, S. Chen, L. Ma, et al., Mater. Today Energy 20 (2021) 100659.
[2] X. Wang, X. Yang, H. Liu, et al., Small Struct. 3 (2022) 2100103.
[3] X. Zhao, X. Yu, S. Xin, et al., Appl. Catal. B: Environ. 301 (2022) 120785.
[4] M.A. Ahsan, T. He, J.C. Noveron, et al., Chem. Soc. Rev. 51 (2022) 812–828.
[5] X. Guo, W. Zhang, J. Shi, et al., Nano Res. 15 (2021) 2092–2103.
[6] H. Yang, B. Wang, S. Kou, et al., Chem. Eng. J. 425 (2021) 131589.
[7] Y. Niu, M. Xiao, J. Zhu, et al., J. Mater. Chem. A 8 (2020) 9177–9184.
[8] J. Wang, F. Ciucci, Appl. Catal. B: Environ. 254 (2019) 292–299.
[9] C. Jing, X. Song, K. Li, et al., J. Mater. Chem. A 8 (2020) 1697–1708.
[10] J. Cheng, H. Zhang, H. Wang, et al., Adv. Funct. Mater. 32 (2022) 2201129.
[11] K. Ge, S. Sun, Y. Zhao, et al., Angew. Chem. Int. Ed. 60 (2021) 12097–12102.
[12] Y. Zhou, R. Abazari, J. Chen, et al., Coord. Chem. Rev. 451 (2022) 214264.
[13] H.F. Wang, L. Chen, H. Pang, et al., Chem. Soc. Rev. 49 (2020) 1414–1448.
[14] A.M. Andrade, Z. Liu, S. Grewal, et al., Dalton Trans. 50 (2021) 5473–5482.
[15] J. Shi, F. Qiu, W. Yuan, et al., Chem. Eng. J. 403 (2021) 126312.
[16] S.H. Lee, J. Kim, D.Y. Chung, et al., J. Am. Chem. Soc. 141 (2019) 2035–2045.
[17] J.B. Pang, R.G. Mendes, A. Bachmatiuk, et al., Chem. Soc. Rev. 48 (2019) 72–133.
[18] J.Y. Qiao, L.Q. Kong, S.K. Xu, et al., Energy Stor. Mater. 43 (2021) 509–530.
[19] T. Shang, Z. Lin, C. Qi, et al., Adv. Funct. Mater. 29 (2019) 1903960.
[20] C. Liu, Y. Bai, W. Li, et al., Angew. Chem. Int. Ed. 61 (2022) e202116282.
[21] G. Zuo, Y. Wang, W.L. Teo, et al., Angew. Chem. Int. Ed. 59 (2020) 11287–11292.
[22] Y. Deng, T. Shang, Z. Wu, et al., Adv. Mater. 31 (2019) 1902432.
[23] M. Naguib, V.N. Mochalin, M.W. Barsoum, et al., Adv. Mater. 26 (2014) 992–1005.
[24] D. Zhao, R. Zhao, S. Dong, et al., Energy Environ. Sci. 12 (2019) 2422–2432.
[25] Z. Fan, Y. Yang, H. Ma, et al., Carbon 186 (2022) 150–159.
[26] D. Xiong, S. Huang, D. Fang, et al., Small 17 (2021) 2007442.
[27] P. Zhang, R.A. Soomro, Z. Guan, et al., Energy Stor. Mater. 29 (2020) 163–171.
[28] X. Li, J. Zhou, C. Liu, et al., Appl. Catal. B: Environ. 298 (2021) 120578.
[29] Q. Shi, Q. Liu, Y. Zheng, et al., Energy Environ. Mater. 5 (2021) 515–523.
[30] X. Li, J. Wei, Q. Li, et al., Adv. Funct. Mater. 28 (2018) 1800886.
[31] S.H. Ahn, A. Manthiram, Small 13 (2017) 1702068.
[32] J. Li, X. Hong, Y. Wang, et al., RSC Adv. 10 (2020) 26834–26842.
[33] X. Zhang, A. Wu, X. Wang, et al., J. Mater. Chem. A 6 (2018) 17905–17914.
[34] T. Wang, Y. Jiang, Y. Zhou, et al., Appl. Surf. Sci. 442 (2018) 1–11.
[35] L. Yan, Y. Xu, P. Chen, et al., Adv. Mater. 32 (2020) 2003313.
[36] Y. Li, Y. Liu, Q. Qian, et al., Energy Stor. Mater. 28 (2020) 27–36.
[37] H. Liu, J. Guan, S. Yang, et al., Adv. Mater. 32 (2020) 2003649.
[38] W. Liu, B. Ren, W. Zhang, et al., Small 15 (2019) 1903610.
[39] N. Wang, S. Ning, X. Yu, et al., Appl. Catal. B: Environ. 302 (2022) 120838.
[40] Q. Dong, H. Wang, J. Ren, et al., Chem. Eng. J. 442 (2022) 136128.
[41] J. Chen, C. Fan, X. Hu, et al., Small 15 (2019) 1901518.
[42] S. Sun, X. Zhou, B. Cong, et al., ACS Catal. 10 (2020) 9086–9097.
[43] W. Gou, J. Bian, M. Zhang, et al., Carbon 155 (2019) 545–552.
[44] C. Wang, H. Lu, Z. Mao, et al., Adv. Funct. Mater. 30 (2020) 2000556.
[45] W. Jin, J. Chen, B. Liu, et al., Small 15 (2019) 1904210.
[46] H. Zhang, Z. Yang, X. Wang, et al., Nanoscale 11 (2019) 17384–17395.
[47] K. Wu, L. Zhang, Y. Yuan, et al., Adv. Mater. 32 (2020) 2002292.
[48] X. Tang, R. Cao, L. Li, et al., J. Mater. Chem. A 8 (2020) 25919–25930.